



Lattice Boltzmann simulations of a pitch-up and pitch-down maneuver of a chord-wise flexible wing in a free stream flow

Dewei Qi, Guowei He, and Yingming Liu

Citation: *Physics of Fluids* (1994-present) **26**, 021902 (2014); doi: 10.1063/1.4866182

View online: <http://dx.doi.org/10.1063/1.4866182>

View Table of Contents: <http://scitation.aip.org/content/aip/journal/pof2/26/2?ver=pdfcov>

Published by the [AIP Publishing](#)

Articles you may be interested in

[Numerical study on the power extraction performance of a flapping foil with a flexible tail](#)
Phys. Fluids **27**, 013602 (2015); 10.1063/1.4905537

[Nonlinear development and secondary instability of traveling crossflow vortices](#)
Phys. Fluids **26**, 064104 (2014); 10.1063/1.4883256

[Aerodynamic effects of wing corrugation at gliding flight at low Reynolds numbers](#)
Phys. Fluids **25**, 071905 (2013); 10.1063/1.4813804

[Three-dimensional flow structure and aerodynamic loading on a revolving wing](#)
Phys. Fluids **25**, 034101 (2013); 10.1063/1.4794753

[Simulations of dynamics of plunge and pitch of a three-dimensional flexible wing in a low Reynolds number flow](#)
Phys. Fluids **22**, 091901 (2010); 10.1063/1.3481786



Lattice Boltzmann simulations of a pitch-up and pitch-down maneuver of a chord-wise flexible wing in a free stream flow

Dewei Qi,^{1,a)} Guowei He,² and Yingming Liu³

¹*Department of Chemical and Paper Engineering, Western Michigan University, Kalamazoo, Michigan 49008, USA*

²*LNM, Institute of Mechanics, Chinese Academy of Sciences, Beijing 100080, China*

³*Yangtze Center of Mathematics, Sichuan University, Chengdu 610064, China*

(Received 25 July 2013; accepted 4 February 2014; published online 26 February 2014)

A rapid pitch-up and pitch-down maneuver of a chord-wise flexible wing in a steady free stream is studied by using a lattice Boltzmann flexible particle method in a three-dimensional space at a chord based Reynolds number of 100. The pitching rates, flexibility, and wing density are systematically varied, and their effects on aerodynamic forces are investigated. It is demonstrated that the flexibility can be utilized to significantly improve lift forces. The flexible wing has a larger angular momentum due to elasticity and inertia and generates a larger leading edge vortex as compared with a rigid wing. Such lift enhancement occurs mainly during the pitch-down motion while a large stall angle is produced during the pitch-up motion. At a low pitch rate, the flexibility cannot improve lift. © 2014 AIP Publishing LLC. [http://dx.doi.org/10.1063/1.4866182]

I. INTRODUCTION AND BACKGROUND

Mechanisms of biologically inspired insects flight have recently become an important research subject, particularly, for use in micro-scale vehicles for defense surveillance and environmental monitoring. Recently, the two-segment beam model in a two-dimensional (2D) space¹ has been extended to a multi-segment beam model in a three-dimensional space by Qi *et al.*^{2,3} They demonstrated that as the number of the beam segment increases, the multi-segment beam model can approximate the nonlinear Euler-Bernoulli beam equation and that the model, incorporated with lattice Boltzmann (LB) method, is suitable for simulation of aerodynamics associated with a flexible wing. This method is called lattice Boltzmann flexible particle method (LBFPM).

Using the LBFPM a numerical simulation of sinusoidal plunge and pitch of a span-wise flexible and a chord-wise flexible wing in hover without free-stream were conducted, respectively.^{3,4} It was found that span-wise and chord-wise flexibility could significantly improve lift forces due to a mixture of five mechanisms: wake capture, rotational,⁵ leading edge vortices (LEV),⁶ wing and fluid inertia, downwash flow leading a smaller effective angle of attach.

However, due to the complex interactions between large deformation and fluid flows, the question “to what extent and how does the flexibility affect each mechanism” is still open and remains a great challenge. To distinguish and quantify the different contribution from each of the five mechanisms to lift and drag forces due to flexibility, the kinematics of wing flapping should be simplified. It is possible that a pitch motion may be isolated from periodic plunge motion. A canonical kinematics with a pitch-up and pitch-down without periodic motion was suggested and used experimentally and numerically for rigid wings by many authors.^{7–13} Such simplicity allows us to focus on the effects of pitch only without considering the influence of the periodic plunge motion. This scheme may effectively reduce the number of variables and the degree of the difficulty in exploring all of the possible mechanism of aerodynamics, in particular, for a flexible wing. Only after understanding

^{a)}Corresponding author. Email address: dewei.qi@wmich.edu

the pitch effect and its relationship with flexibility whole physical picture of complexity of flapping flight will be more easily captured and understood.

Recent, Kilany *et al.*¹⁴ measured the structures of leading and trailing edge vortices (TEV) of flat plate undergoing pitch-ramp motion at Reynolds number 7500. It was found that positive trailing edge vortices were identified in the earlier stage of the pitch-up and negative trailing edge vortices were seen at the end of the pitch-down motion. A large coherent leading edge vortex was formed at the beginning of the pitch-up. Ol *et al.*¹⁵ used particle image velocimetry (PIV) and dye injection to measure vortices at Reynolds number 10 000 and found that increasing pitch rate leads to a tighter, more coherent leading edge vortex, which lifts off further from the airfoil suction side; and to a stronger trailing edge vortex system, which rolls up into a counter-rotating vortex pair. They also computed the lift force using a viscous vortex particle method in a two-dimensional model and found that on the pitch-up, lift coefficient normalized by the pitch rate collapsed to essentially one curve, for the pitch rate $\kappa \sim 0.35$. However, on the pitch-down, no such simple collapse was obtained. Buchmann *et al.*¹⁶ and Yilmaz and Rockwell¹⁷ measured the fluid structures and they observed large span-wise velocities in the fluids of the Reynolds number of 7500 and 10 000. Jantzen *et al.*¹⁸ used an immersed boundary projection method to investigate the vortical structures and the influence of the span to chord ratio of a flat wing in the Reynolds number range 14–500. In particular, Visbal¹⁹ as well as Garman and Visbal²⁰ used high-order Navier-Stokes solver FDL3D²¹ to investigate the dynamic stall characteristics in three-dimensional space in the range of Reynolds number 1000–4 × 10⁴ and pitch rate $\kappa = 0.05\text{--}0.2$. Visbal¹⁹ found that as pitch rate or Reynolds number increases a more compact arch vortex system, a stronger circulatory pattern and lower pressures above the wing surface, increased maximum lift, and delay of stall were evident.

All studies above are limited to a rigid wing. To authors' knowledge, there is no report on pitch-up, hold, and pitch-down motion of a three-dimensional flexible wing. This motion is somewhat representative of biological perching. Therefore, in the present work, the canonical kinematics are adopted to simulate a chord-wise flexible wing embedded in a free stream at a Reynolds number of 100, which is within the range of insect flight. This study utilizes the same LBFPM as investigated by Qi *et al.*^{3,4} to examine how flexibility affects lift and drag forces as well as fluid structures at different pitch rates.

Section II will briefly introduce the simulation method and the canonical kinematics. Section III will present the results of the influence of flexibility on lift and drag forces at different conditions. The conclusions will be made in Sec. IV.

II. SIMULATION METHOD

It is well known that the Navier-Stokes equation can be solved by using lattice Boltzmann method. In general, the algorithm of the LB method for simulating a fluid domain is extremely simple and consists of only two operations, collision and streaming. It has been demonstrated that the LBFPM is particularly suitable for simulations of flexible bodies in fluid flows. The LBFPM has been reported in details elsewhere by Qi² and Qi *et al.*³ and will not be repeated here. In this method, the body of the wing has been discretized into a chain of rigid beam segments. The segments are connected through ball and socket joints at the segment ends. Bending and twisting of the wing are obtained through relative rotation between neighboring segments. Constraint forces have been introduced at each joint to ensure that the segments are connected to each other. The motion of fluid and its interactions with solid boundaries are handled by the lattice Boltzmann equation. The validation of the LBFPM was extensively provided by comparing its results with the experimental and numerical results of Toomey and Eldredge.¹ It has been demonstrated that the LBFPM is faithful and replicates the correct physics of flow response to deformable either span-wise or chord-wise flexible wing. This method will be used here again.

A flexible wing is subjected to a pitch-up and pitch-down motion in an incompressible fluid with a density of ρ_f and a kinematic viscosity of ν in a free stream flow with a velocity of U_0 .

The wing with a rectangular cross section could be described either in a space-coordinate system (X, Y, Z) or a body-fixed coordinates system. The body-fixed coordinates (X', Y', Z') can be transferred to the space coordinates (X, Y, Z) through the Euler angles ϕ, θ , and ψ ²² if rotation is

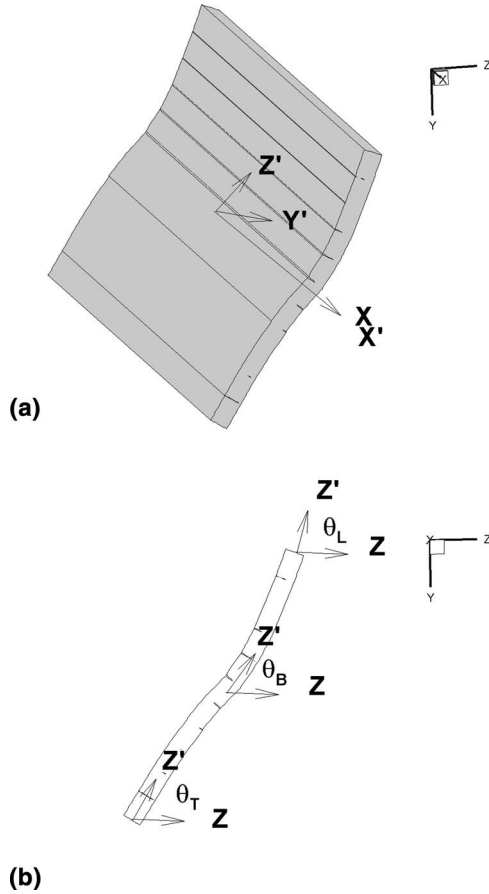


FIG. 1. (a) A 3D setup is shown. The body-fixed coordinate (X', Y', Z') is rotating an angle of θ around the X or X' -axis. The X -axis is always overlapped with the X' -axis. (b) The cross section view in the X -direction; the pitch angle θ is the angle between vectors OZ' and OZ . Leading edge angle θ_L , base angle θ_B , and trailing edge angle θ_T are associated with their own body-fixed coordinates. The base segment is located at the chord center.

imposed. Initially, the body-fixed coordinate system (X', Y', Z') overlaps with the space coordinate system (X, Y, Z). The flexible wing is placed in the center of the simulation box such that the span s is along the X' -direction; the chord c along the Z' -direction; the wing thickness of h along the Y' -direction. The wing is uniformly discretized along the chord as N segments. Thus, the angle θ of the base segment spinning around its X' - or X -axis is the pitch angle or the angle of attack as shown in Figure 1. Following the work of Eldredge,²³ this pitch angle is pre-described and given by

$$\theta(t) = \theta_0 \frac{G(t)}{\max G}, \quad (1)$$

where θ_0 is the maximum of the pitch angle and G describes a complete pitch-up and pitch-down maneuver,

$$G(t) = \ln \left[\frac{\cosh(aU_0(t - t_a)/c) \cosh(aU_0(t - t_d)/c)}{\cosh(aU_0(t - t_b)/c) \cosh(aU_0(t - t_c)/c)} \right]. \quad (2)$$

The parameter a controls the speed of the pitch transition between kinematic intervals, with larger values producing sharper transitions. A moderate value of 11 throughout the present study is used. The time t_a, t_b, t_c, t_d represent transition instances during the maneuver: t_a is the start of the pitch-up, $t_b = t_a + \theta_0/\dot{\theta}_0$ is the end of the pitch-up, $t_c = t_b + \Delta T$ is the start of the pitch-down, and $t_d = t_c + \theta_0/\dot{\theta}_0$ is the end of the pitch-down where $\dot{\theta}_0$ is the pitch rate, c is the chord length. The

TABLE I. Kinematics and wing parameters.

θ_0	U_0	a	ΔT	c/s	h/c
45°	0.044	11	$0.05c/U_0$	2.5	0.06

dimensionless pitch rate κ is defined by

$$\kappa = \dot{\theta}_0 c / (2U_0). \quad (3)$$

This kinematics has been used by Eldredge and Wang²³ for a two-dimensional rigid wing. In the present work, pitch starts at $t_a = c/U_0$, the parameters are fixed at $\theta_0 = 45^\circ$, $\psi = 0^\circ$, $\phi = 0^\circ$, $s/c = 2.5$. The pitch rate is varied at $\kappa = 0.2, 0.7$, and 1.25 . A holding time $\Delta T = 0.05c/U_0$ is used. The wing thickness is fixed at $h = 0.06c$. The parameters of the kinematics and wing structure are collected in Table I. The simulation box size is $(N_x, N_y, N_z) = (250, 300, 300)$ and the wing with $s = 125$ and $c = 50$ is used. A larger simulation box of $(N_x, N_y, N_z) = (334, 400, 400)$ is also used to test the sensitivity of the grid size. The length unit is 1.33 times and the time unit is 1.78 times smaller in the fine grids than in the coarse grids. The curves of the lift and drag forces as a function of time for a flexible wing with an intermediate rigidity of $EI = 0.67$ are compared between the two grids in Figure 2. It shows that the difference of the lift and drag force results as a function of time between the two grids is very small and the average lift coefficient is less than 5%. To save cost, the former box size is used in this work. In addition, lattice Boltzmann simulations are carried out for the same case of $Re = 200$ in Ref. 24 and the results of lift and drag force are compared in Figure 3 with those of Barnes and Visbal,²⁴ who used FDL3D1 method. The results by using the two different methods are very close to each other.

Further, the exact same case as Figure 5 of Eldredge and Wang's²³ article is run in a two-dimensional space by using the lattice Boltzmann method and the results of lift and drag coefficients are compared and presented in Figure 4. A good agreement between the two results shows a validation of the lattice Boltzmann method with the pitch-ramp-return kinematic function.

It was also demonstrated in Ref. 3 that the simulation results had no essential difference for flexible wing hovering case at $Re = 136$ by using the number of the segments ranged from $N = 9$ to 13. In this work, the number of the segments $N = 11$ is selected. The pivot ratio $r_p = 0.5c$ is used throughout this work. The effects of the pivot ratio on lift are not pursued.

In the present work, the chord based Reynolds number is defined by

$$Re = \frac{U_0 c}{\nu}. \quad (4)$$

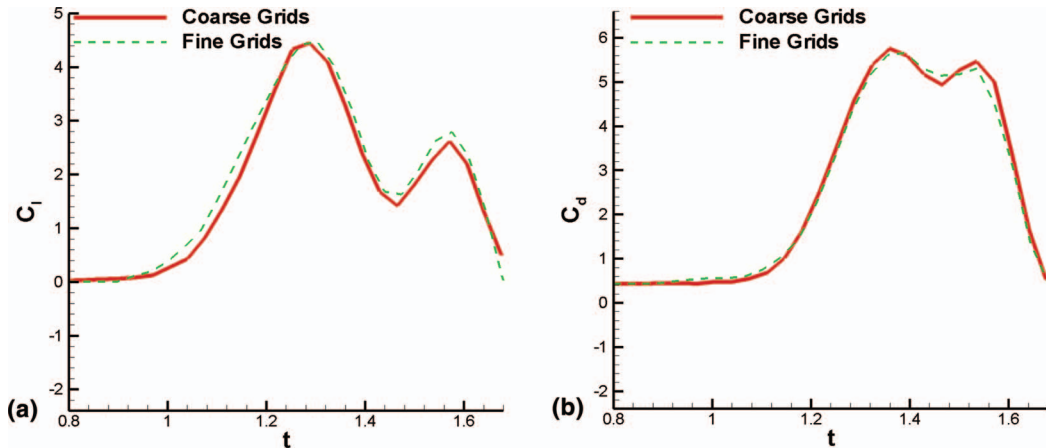


FIG. 2. Simulations are carried out by using two different grids and the results of lift (a) and drag coefficients (b) as a function of time are compared between the two grids for the case of $E = 0.67$.

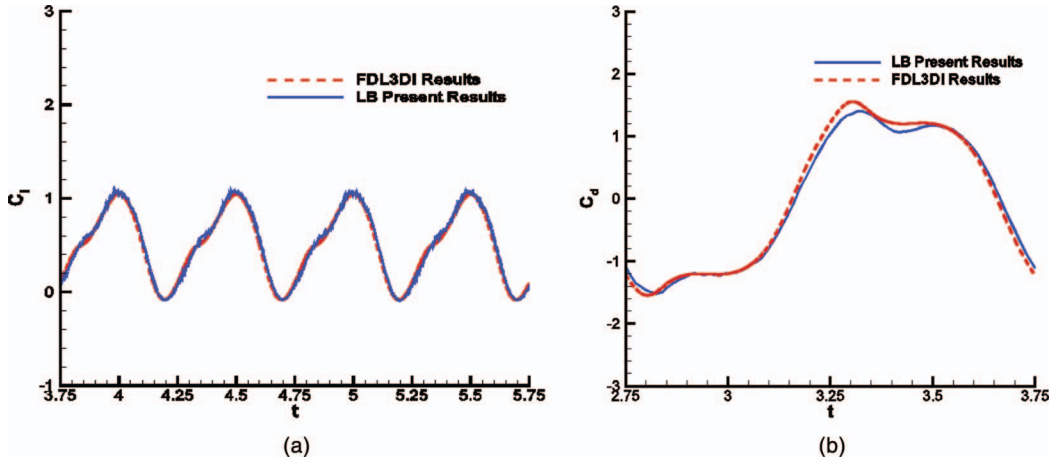


FIG. 3. The lift (a) and drag (b) coefficient of LB simulation results are compared with those of Barnes and Visbal,²⁴ who used FDL3D1, for the case of the rigid wing flapping at $Re = 200$. Grids of $150 \times 340 \times 340$ are used.

The bending flexural rigidity $EI_w = \frac{1}{12}Esh^3$ can be normalized by

$$EI = \frac{EI_w}{\rho_f U_0^2 sc^3}, \quad (5)$$

where E is Young's modulus. Following Ref. 25, the mass ratio of the wing inertia to the fluid dynamic force is defined by $m^* = \rho_s h / \rho_f c$, which varies at three different levels in the simulation.

III. RESULTS

A. Flexibility on lift and drag

To understand effects of flexibility on lift and drag forces, the force coefficients are computed at different levels of the bending flexural rigidity while keeping other conditions same. The results of average lift and drag force coefficients over the pitch up and down time interval as a function of bending flexural rigidity are shown in Figure 5 for the case of pitch rate $\kappa = 1.25$ at the mass ratio $m^* = 1.0$. As the rigidity reduces or the flexibility increases, the lift force increases and arrives at a maximum when the flexibility is at an intermediate level. As the rigidity continuously decreases and

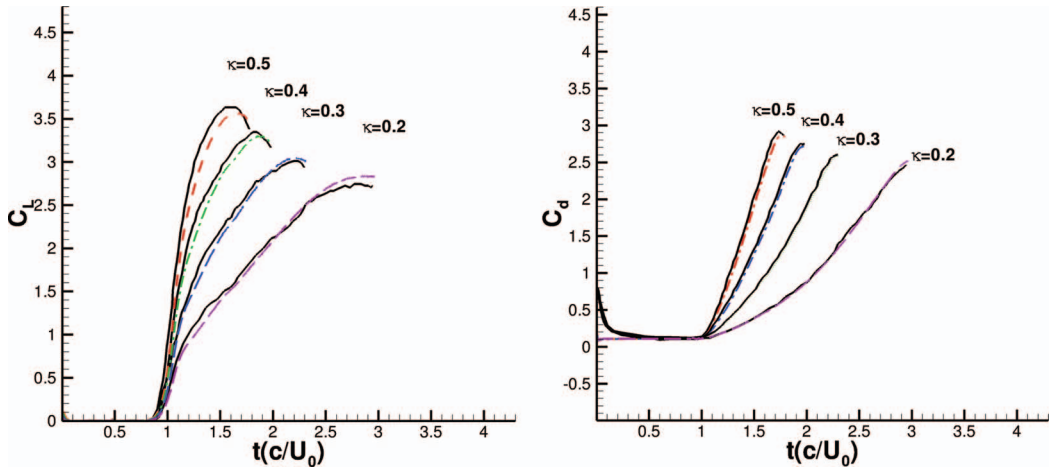


FIG. 4. The LB simulation results (dashed lines) of lift and drag coefficients are compared with those (solid lines) of Eldredge and Wang²³ at $Re = 1000$. Two grids of 2000×2000 and 1600×1600 are used.

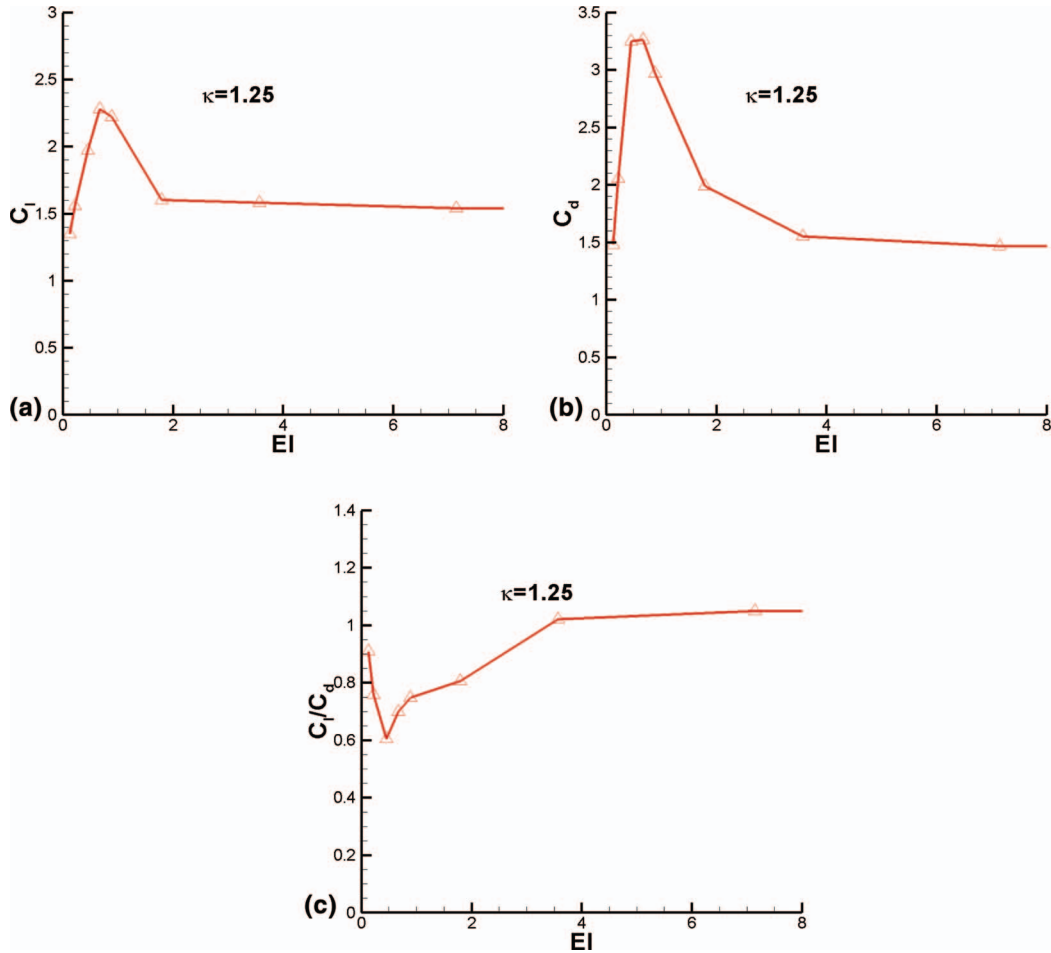


FIG. 5. The lift (a) and drag coefficients (b) as well as the ratio of the lift to the drag coefficient (c) as a function of the rigidity for the case of $\kappa = 1.25$ at the mass ratio $m^* = 1.0$. The data cutoff in the right is due to the infinite large rigidity for the rigid wing.

the wing becomes excessively flexible, the lift falls down. The value of the lift coefficient increases from 1.48 for the rigid wing to 2.28 for the flexible wing of $EI = 0.67$. In other words, with pitch or rotation, the flexibility results in a 54% increase in lift as compared with the rigid wing. The drag force has a similar behavior. It is demonstrated that the flexibility significantly improves the lift forces. The ratio of the lift to the drag coefficient as a function of the rigidity is plotted in Figure 5(c). It is shown that as the rigidity decreases the ratio also decreases, then increases again. There is a minimum in the ratio curve, indicating that the lift increase due to flexibility is at a cost of a drag increase or more power consumption for this simple pitch-up and pitch-down motion. This is what one expects. When a higher lift is maintained, a larger drag is required to slow down rotation during perching motion.

To see more details of dynamic characteristics, the results of the lift and drag coefficients as a function of time within a pitch-up and pitch-down time interval are shown in Figure 6 and compared between the rigid wing and the flexible wing with $EI = 0.67$. The kinematics of pitching angle is also shown in the figure.

There are several interesting observations. First, in the earlier stage of the pitch-up motion ($t < 1.24$), the lift is smaller for the flexible wing than for the rigid wing. This is because the angular velocity or rotational momentum is smaller for the flexible wing due to its inertia that tries to keep the wing's original zero angular velocity at the beginning of the pitch-up motion. The rotational angles of the leading and trailing edges as a function of time are compared between the flexible and

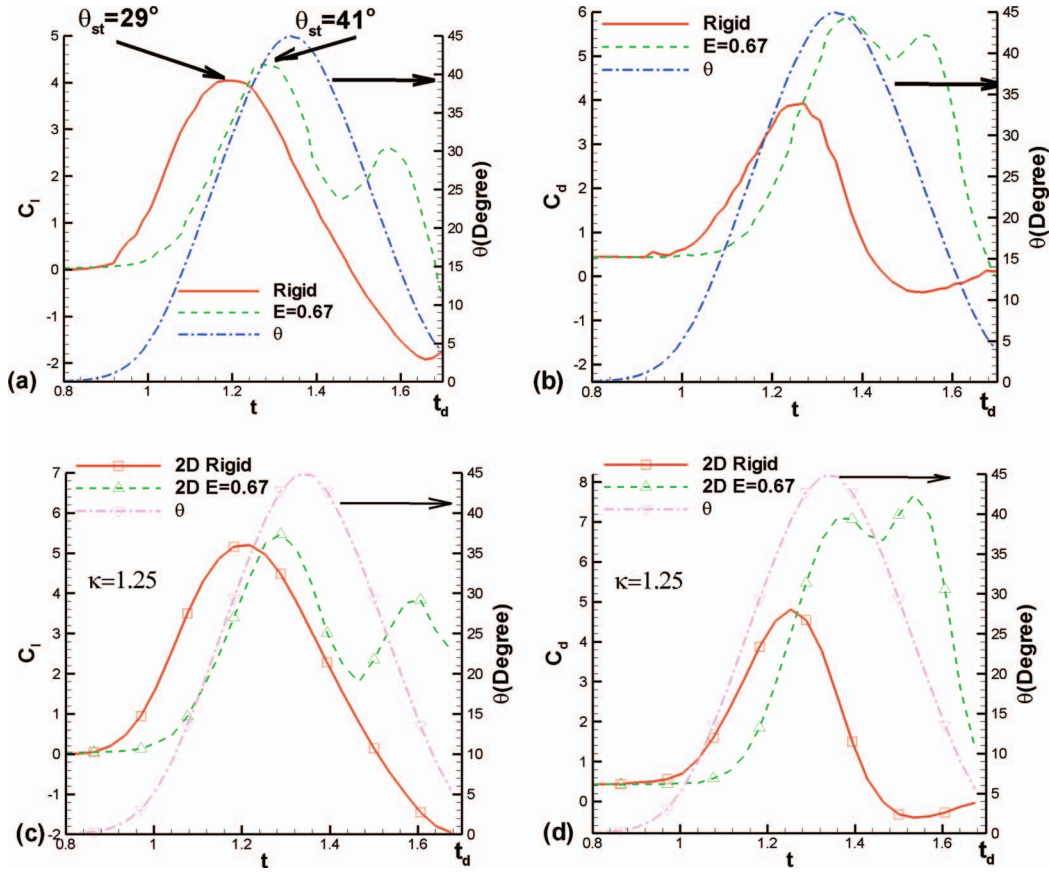


FIG. 6. (a) The lift and (b) drag coefficients as a function of time during the time interval between t_a and t_d are compared between the flexible wing of $EI = 0.67$ corresponding to the rigidity of a Aeshna wing and a rigid wing at $\kappa = 1.25$ and $m^* = 1.0$. Also the results are compared with the two-dimensional results of lift (c) and drag (d). The pitch angle as a function of time is also shown on the right vertical axis where the arrow points to the angle scale. The pitch-up starts at $t = t_a = 1$ and the pitch-down ends at $t = t_d = 1.68$ where the time t is normalized by c/U_0 and the same applies to the rest of this paper.

rigid wings in Figure 7. The smaller angular velocities or slopes of the angle curves of the leading and trailing edges for the flexible wing result in smaller LEV with less suction effects and lead to a smaller lift force (see more in Sec. III C). As the base angle approaches the middle of the pitch-up motion, the angular velocity of the leading and trailing edges of the flexible wing increases and becomes larger than the rigid wing or the base segment (noting that the rigid wing has the same angular function of the time as the base segment of the flexible wing). When the angle of the base segment reaches its maximum angle $\theta = 45^\circ$, the base rotation is stopped at $t = t_b = 1.314$. However, at this instance the flexible leading and trailing edges are not stopped and continue to rotate due to their inertia. The angle of the leading edge continuously grows with a larger angular velocity until the leading edge angle arrives at its maximum value $\theta_L = 92^\circ$ at a later time $t = 1.47$. At this instance, the base segment has already passed its maximum for a while and its angle has reduced to $\theta_B = 37^\circ$ so that a large deformation angle $\delta\theta = \theta_L - \theta_B = 54^\circ$, with respect to the base angle, is obtained for the leading edge. After passing the maximum of the leading edge angle where the rotational velocity is zero, the elastic restoring force due to the large deformation will drive the leading edge to acceleringly swing back and creates a larger angular velocity as the leading edge angle passes its equilibrium angle as shown in Figure 7. The larger rotation momentum results in a larger LEV (see more later), which causes a larger force for the flexible wing with large angles of attack at $t = 1.36$ through $t = 1.65$, as shown in Figures 7 and 8, despite the large angles of attack may encourage LEV separation and reduce lift force for a static wing case. The angle of the trailing edge has a similar behavior to the leading edge.

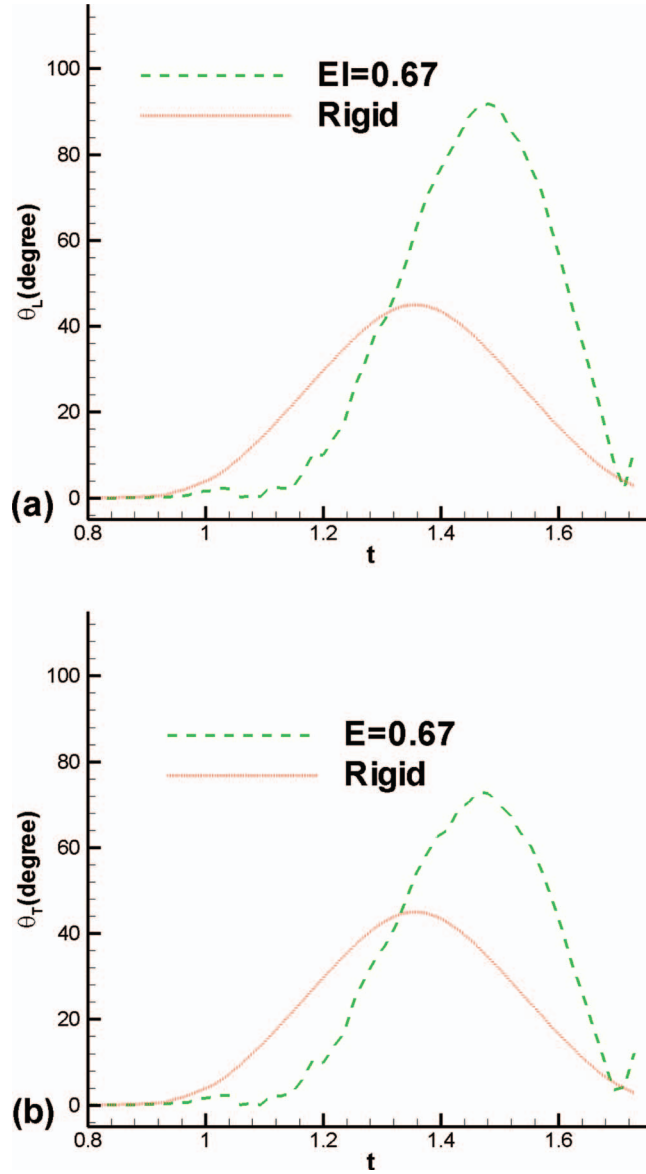


FIG. 7. The leading edge angle θ_L (a) and the trailing edge angle θ_T (b) as a function of time are compared between the flexible and rigid wing. The magnitudes of the slopes of the angular curves are larger for the flexible wing than for the rigid wing the most time during the pitch-down motion.

It is meaningful to visualize the relationship between the deformation and the force on the wing. The results of the chord deformation and the force vectors on the flexible wing of $EI = 0.67$ and $m^* = 1.0$ are compared with the corresponding rigid wing in Figure 8 at different time instances, $t = t_1 = 1.02$ through $t = t_{16} = 1.65$. The time interval between two consecutive time instances is $\Delta t = 0.04$. The figure shows that the magnitudes of the force vectors are smaller for the flexible wing (blue arrows) than for the rigid wing (red color) at time $t = t_1 = 1.02$ through $t = t_5 = 1.19$ in the earlier stage of the pitch motion. However, the lift force becomes larger for the flexible than for the rigid wing when $t > 1.24$ and the large lifts are associated with the large angular deflection at $t = t_9 = 1.36$ through $t = t_{16} = 1.65$ as shown in Figure 8.

Second, there are two peaks and one valley between the two peaks in the force curves of the flexible wing while there is one peak only for the rigid wing. The second peak of the flexible wing is mainly caused by a combination effects of wing elasticity and inertia. As the flexible wing

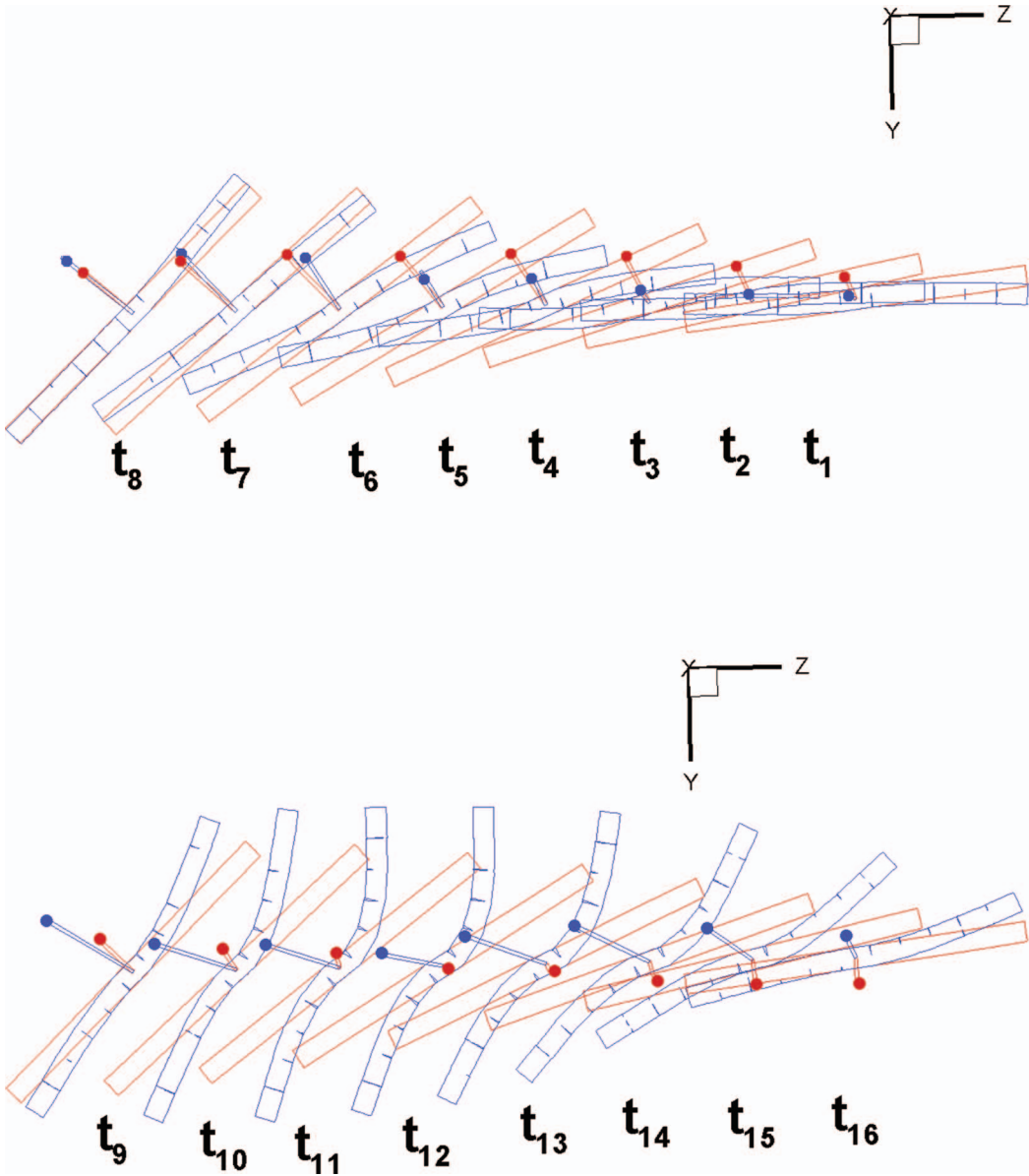


FIG. 8. The chord deformation and the force vectors (blue color arrows) for the flexible wing of $EI = 0.67$ are compared with those of the flexible rigid wing (red color) at different time instances $t = t_1 = 1.02$ through $t = t_{16} = 1.65$. The different positions correspond to the different time instances labeled. The time interval between two consecutive instances is $\Delta t = 0.04$.

leading edge angle reaches its maximum, a zero rotational speed is obtained around $t = 1.47$ and a valley in the lift curve appears. After passing this moment, the elastic restoring force drives the leading edge to acceleringly swing back and results in a larger rotational velocity although air flow may resist the wing elastic motion. Therefore, the lift increases again and the second peak occurs at an equilibrium bending angle corresponding to a maximum bending rotational velocity around $t = 1.57$, then the lift reduces again after passing the equilibrium bending angle. The rigid wing lacks such elastic bending mechanisms, therefore the lift curve has one peak only.

Third, it is remarkable that during the pitch-up motion the lift maximum, where the angle of attack corresponds to a stall angle θ_{st} , occurs at $\theta_{st} = 41^\circ$ for the flexible wing and at $\theta_{st} = 29^\circ$ for the rigid wing, revealing that the stall is greatly delayed by the flexibility. Moreover, the lift maximum is larger for the flexible than rigid wing.

Fourth, the lift coefficient of the rigid wing reduces monotonically from a maximum $C_l = 4.04$ at $t = 1.18$ to a negative value at $t = 1.48$ and continuously reduces to a large negative value of $C_l = -1.9$ at the end of the pitch-down motion. On the contrary, the lift coefficient of the flexible wing decreases from the maximum $C_l = 4.39$ at $t = 1.27$ to the minimum (valley) $C_l = 1.50$ at $t = 1.47$, increases again to the second peak $C_l = 2.6$ at $t = 1.57$ and remains a positive value of $C_l = 0.49$ at the end of the pitch-down motion where the rotation is stopped (see Figure 6(a)). The lift coefficient is always larger for the flexible than for the rigid wing when $t > 1.24$.

Fifth, Figure 7 shows that the angles of both the leading and trailing edges of the flexible wing are much larger than the base angle in the late portion of the pitch-up time period and in all the pitch-down time period. The maximum angle of the flexible leading edge is as large as 92° at $t = 1.47$ where the lift is still positive $C_l = 1.41$. Undoubtedly, it is clearly depicted that not only the lift is significantly increased but also the stall is effectively delayed by the enhanced unsteady dynamics due to the flexibility and wing inertia.

Finally, it can be seen in Figure 6 that the peaks of the force curves of the rigid wing have a phase lead to the pitch angle function as expected. The phase lead is due to the acceleration peak (added mass) of the rotation (or pitch) that appears in the very earlier stage of the time in the pitch-ramp-return function. This has been clearly explained by Ol *et al.* (see Figure 2 of Ref. 7). The peaks of the force curves of the flexible wing shift to the right side as compared with the rigid wing. This phase shift or delay is due to flexibility since the motion of the wing edges is driven by the base segment and transferred from the wing base to the wing edges.

A two-dimensional simulation is carried out in the same condition except that the length of the simulation box in the span-direction is the same as the wing span and the periodic condition is imposed in this direction so that a three-dimensional simulation reduces to two-dimensional, which has a infinitely large span. The lift and drag forces are shown and compared between the flexible and rigid wings in Figures 6(c) and 6(d). The values of the 2D results of the lift and drag are reasonably larger than three-dimensional results due to less dissipation in the span direction. Similar to the three-dimensional case, the stall angle is $\theta_{st} = 43^\circ$ for the 2D flexible wing and $\theta_{st} = 34^\circ$ for the 2D rigid wing and the stall is effectively delayed by the flexibility. The lift curve has two peaks and the maximum of the lift is larger than the rigid wing. Although the flexibility improves lift, tip vortices are not obtained in our 2D simulations, as expected (see Sec. III C).

It is pointed out that the inertial effect includes a contribution from the air flow, around the wing surface boundary layers, which moves along with wing motion and contributes to an extra inertia called “added mass.” Fluid viscous effect may also resist or damp the angle change of the leading and trailing edges.

To examine effects of flexibility on the lift force and deformation, simulations are carried out in the different levels of the rigidity in the same condition. The results of lift and drag coefficients and leading and trailing edge angles at different levels of the rigidity are plotted in Figure 9 at a given pitch rate $\kappa = 1.25$ and a given mass ratio $m^* = 1.0$. All the curves have similar characteristics. Two findings are noted. First, the pitch angles corresponding to the maximum of the lift curves are larger for all the flexible wings than for the rigid wing. The wing with $EI = 0.89$ has a maximum lift $C_l = 4.46$ at a stall angle $\theta_{st} = 39^\circ$; the wing with $E = 0.67$ has a maximum lift force $C_l = 4.39$ at a stall angle $\theta_{st} = 41^\circ$; the wing with $E = 0.45$ has a maximum lift force $C_l = 4.05$ at a stall angle $\theta_{st} = 45^\circ$. In other words, the first lift maxima and stall angles are larger for all the considered flexible wings than for the rigid wing. Second, all the lift curves of flexible wings have two peaks. The peaks shift to the side of the late time or the first and second peaks are delayed as the rigidity reduces or the flexibility increases as shown in Figure 9(a). The deformation or leading and trailing angles increase as the flexibility increases as shown in Figure 9(c) and 9(d). The peak delay is attributed to the larger angular deflection, which takes a longer time.

B. Effect of pitch rate

To investigate the effect of pitch rate on forces, the pitch rate is varied in three different levels $\kappa = 0.2, 0.7$, and 1.25 . The results of the lift and drag coefficients as a function of time at given mass ratio $m^* = 1.0$ and rigidity $EI = 0.45$ are plotted and compared in Figure 10 among the three different

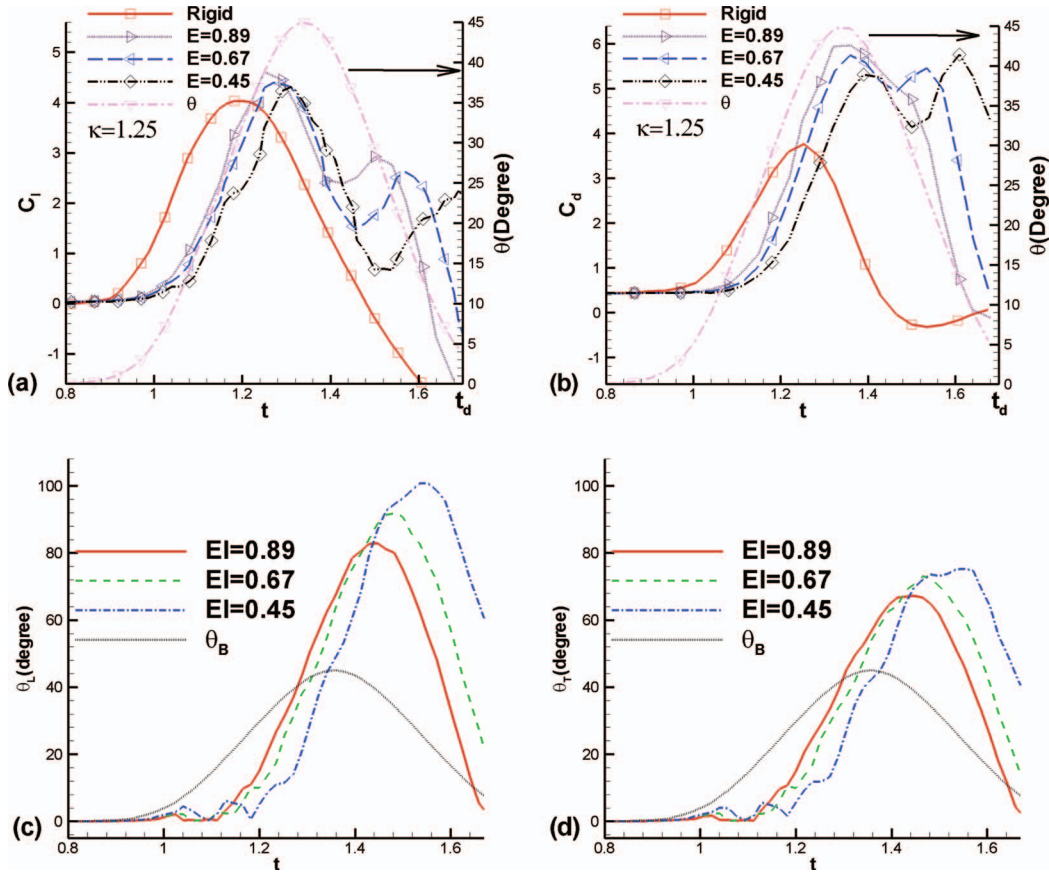


FIG. 9. The (a) lift, (b) drag coefficients, (c) leading edge angle, and (d) trailing edge angle as a function of time during the time interval between t_a and t_d are compared among the three different levels of the rigidity of flexible wing at given $\kappa = 1.25$ and $m^* = 1.0$. The pitch angle as a function of time is also shown on the right vertical axis where the arrow points to the angle scale.

pitch rates $\kappa = 0.2, 0.7$, and 1.25 . Their corresponding deformations are compared in Figure 11. Figure 10 shows that the lift and drag increase as the pitch rate increases by noting the force scales are different among the cases of $\kappa = 0.2, 0.7$, and 1.25 . When pitch rates are large, the lift curves of the flexible wings have two peaks and the first peak or the stall angles are delayed as compared with the rigid wing. For example, when $\kappa = 0.7$, the maximum value of lift is 3.87 at the stall angle $\theta_{st} = 42^\circ$ for the flexible wing while the maximum of the lift is 2.61 at the stall angle $\theta_{st} = 34^\circ$ for the rigid wing. As the pitch rate increases to $\kappa = 1.25$, the maximum value of lift increases to 4.3 at a larger stall angle $\theta_{st} = 44^\circ$ for the flexible wing while the maximum of the lift is 4.04 at the stall angle $\theta_{st} = 29^\circ$ for the rigid wing. However, when the pitch rate is small, say $\kappa = 0.2$, the lift force and stall angle are not larger for the flexible wing. It seems that the benefit from flexibility is not clearly observed for this low pitch rate. There are a few small peaks in the lift curve of the flexible wing. These peaks may be explained by natural frequency of a flexible beam vibration. The period of the vibration is roughly around 0.7 in the simulations, which is close to theoretical value 0.67 according to the beam theory.²⁶

The time average of lift and drag, are plotted as a function of rigidity at three different pitch rates $\kappa = 1.25, 0.7$, and 0.2 in Figure 12. It is shown that at a given mass ratio, all the lift force curves have a maximum and that the maximum significantly increases as the pitch rate increases. Therefore, the lift force curves have a maximum for $\kappa = 1.25$ and 0.7 . On the contrary, there is no clear maximum in the lift curve for the case with the low pitch rate $\kappa = 0.2$. Obviously, a high

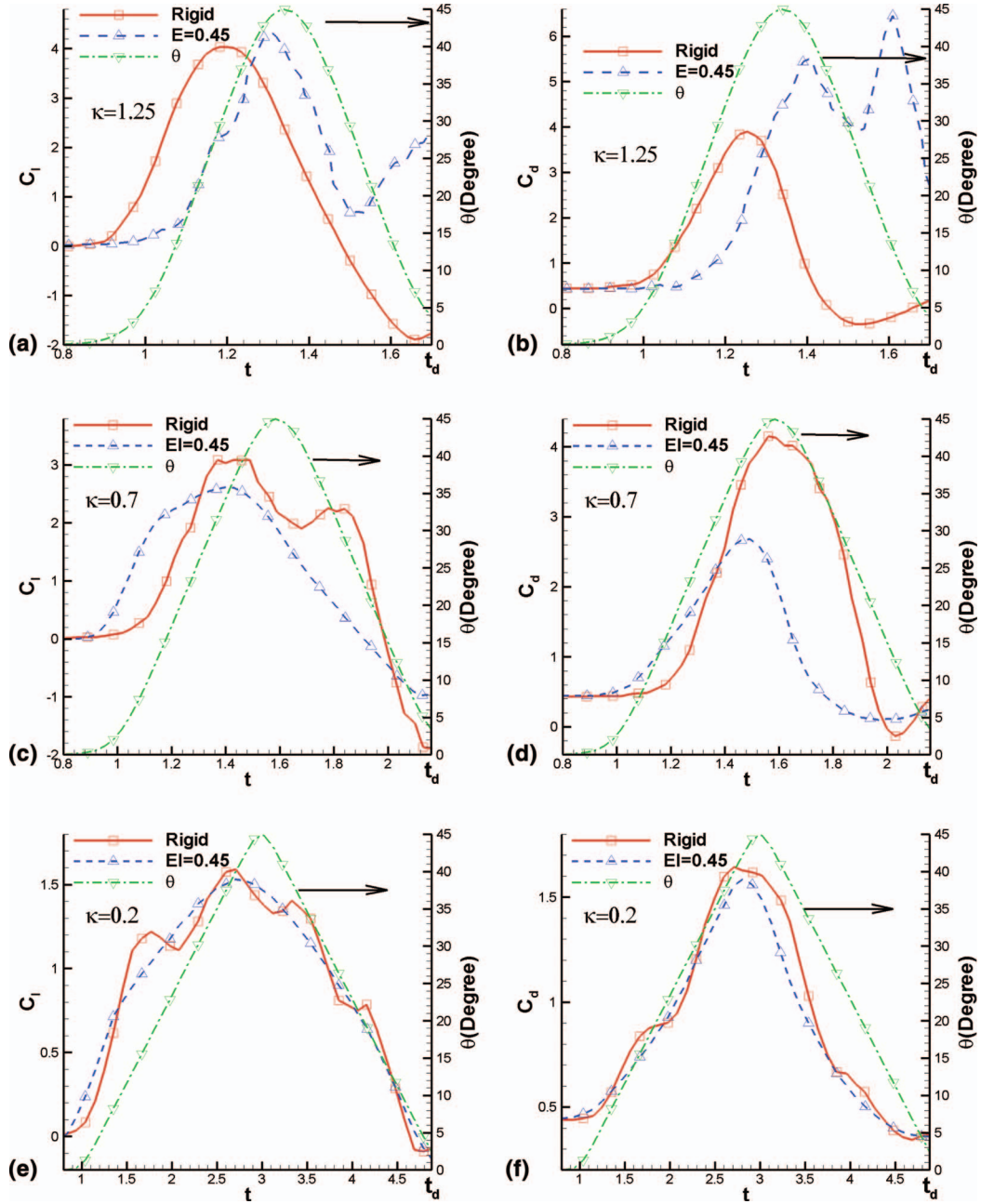


FIG. 10. (a) Lift and (b) drag coefficients as a function of time for $\kappa = 1.25$, (c) lift and (d) drag for $\kappa = 0.7$, and (e) lift and (f) drag for $\kappa = 0.2$ are compared at given mass ratio $m^* = 1.0$ and rigidity $EI = 0.45$.

pitch rate is critical for insects to use flexibility to generate a larger lift force. The drag has a similar behavior except that the drag force also has a maximum for the case of $\kappa = 0.2$.

C. Structures of fluid

To see how fluid structures affect lift force, the contours of the vorticity in the x-direction in the cross section at the span ratio $s_r = 0.25$ are compared between the flexible wing of $EI = 0.67$ and the rigid wing at different time instances in Figure 13. The intensity and the size of the LEV is smaller for the flexible wing than the rigid wing due to the wing inertia keeping its original zero speed in the

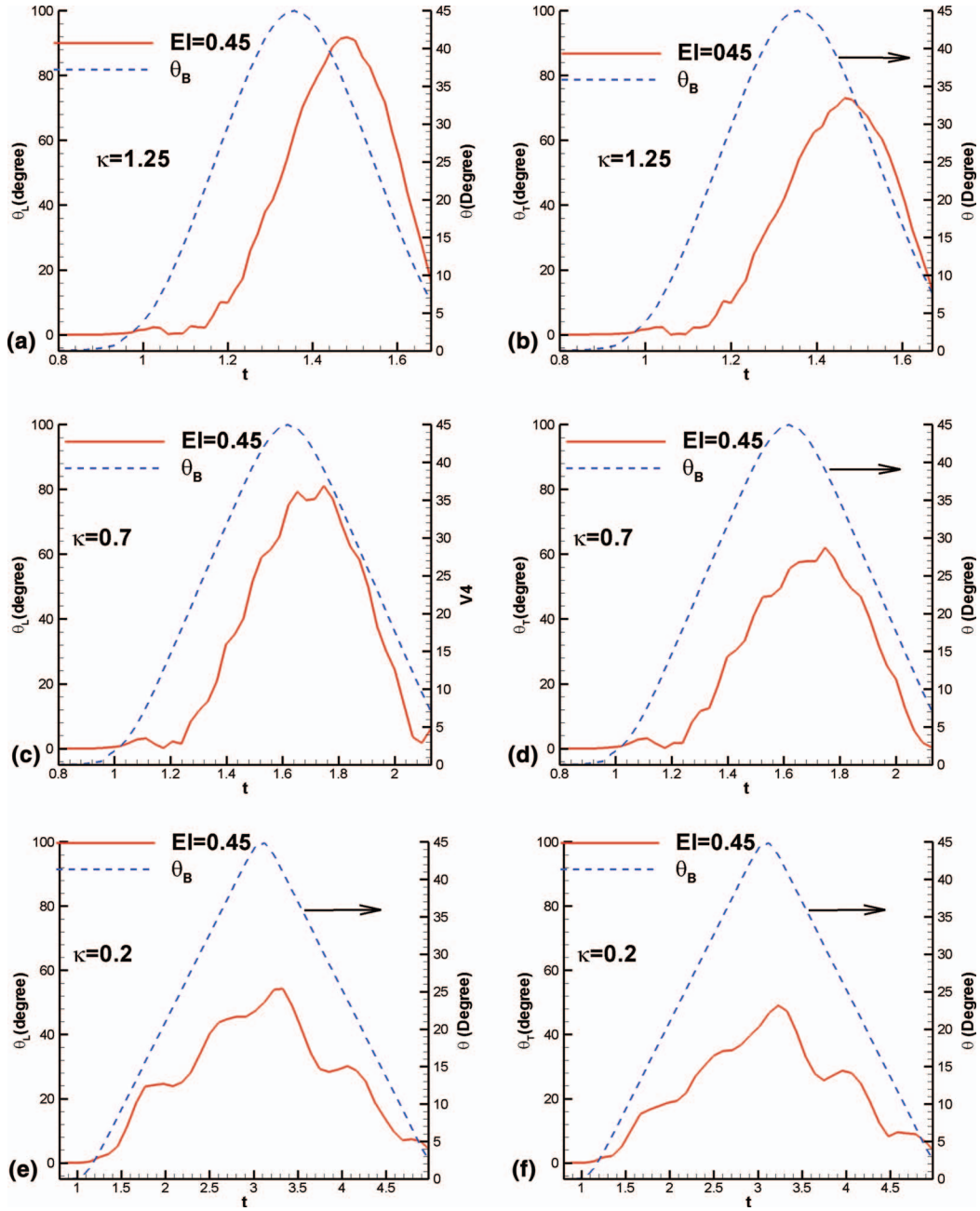


FIG. 11. (a) Leading edge angle and (b) trailing edge angle as a function of time for $\kappa = 1.25$; (c) leading edge angle and (d) trailing edge angle for $\kappa = 0.7$; (e) leading edge angle and (f) trailing edge angle for $\kappa = 0.2$ are compared. The mass ratio $m^* = 1.0$ and the rigidity $EI = 0.45$ are given.

earlier stage of pitch-up motion as shown in this figure at $t = 1.06$ and $t = 1.14$ so that the flexible wing has smaller lift force. When the base pitch angle $\theta = 41^\circ$ at $t = 1.27$, not only the intensity but also the size of the LEV is larger for flexible wing than for the rigid wing. The LEV covers all the surface of the flexible wing while the LEV has started to separate from the leading edge for the rigid wing. When the base pitch angle $\theta = 45^\circ$ at $t = 1.36$, the LEV still covers 80% of the top surface of the flexible wing but the LEV is clearly separated from the leading edge for the rigid wing. A comparison reveals that the vorticity field for the flexible wing at $t = 1.48$ looks strikingly similar to that of the rigid wing at $t = 1.36$, indicating that the LEV separation is effectively delayed

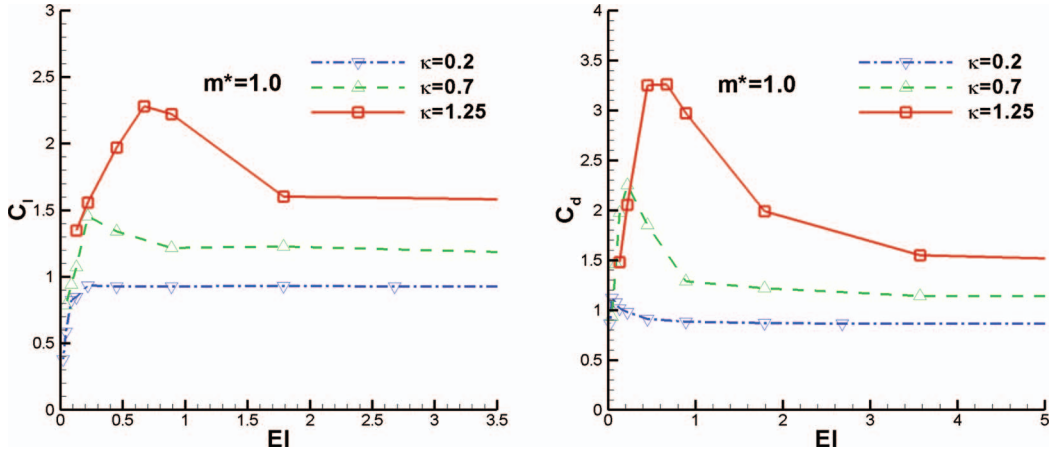


FIG. 12. The lift (left) and drag (right) coefficients as a function of rigidity at the different pitch rates $\kappa = 0.2, 0.7$, and 1.25 for a given mass ratio $m^* = 1.0$.

due to flexibility and the LEV is stabilized. In other words, the lag in the vortex development and separation due to flexibility allows the LEV to have a longer time to be attached on the top surface. At $t = 1.27, 1.36$, and 1.65 , larger LEV are observed for the flexible wing.

Distinguishing feature of the three-dimensional fluid flows is that tip vortices are presented. As an example, Figure 14(a) shows the contours of the vorticity in the chord-wise direction or z-direction on the cross section of chord ratio $r_p = 0.85$. Each vortex on the wing tips has opposite sign. The span-wise velocities, associated with the tip vortices, are shown in in Figure 14(b). Two-dimensional flows do not have such tip vortices in our simulation results.

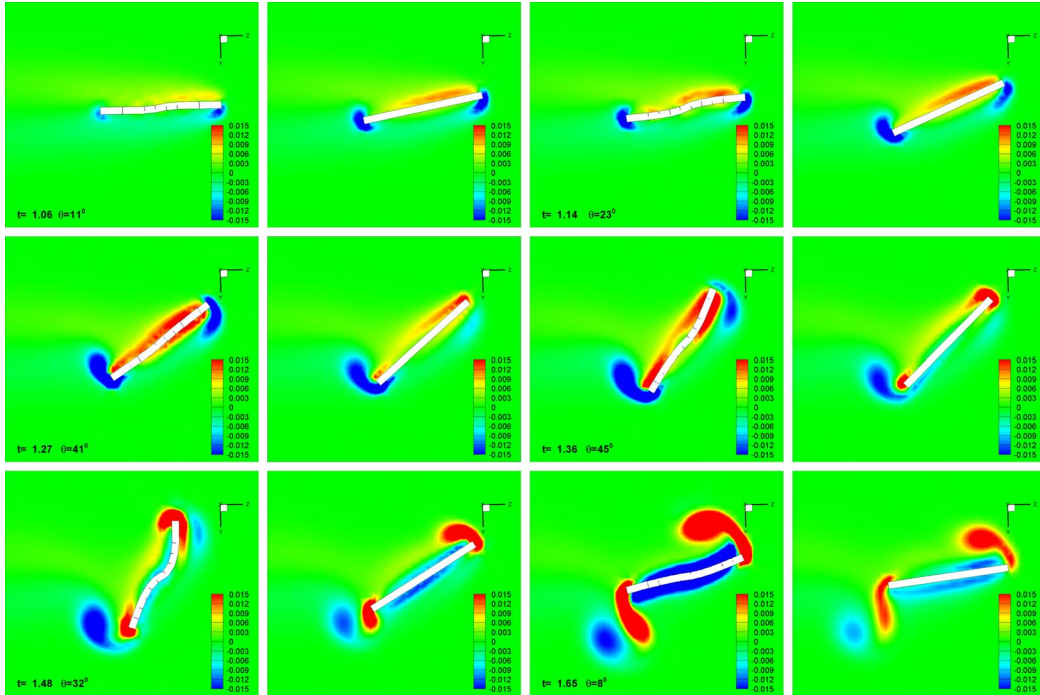


FIG. 13. The contours of the vorticity in the x-direction in the cross section at $s_r = 0.25$ are compared between the flexible wing (first and third columns) of $EI = 0.67$ and the rigid wing (second and fourth columns) at different time instances.

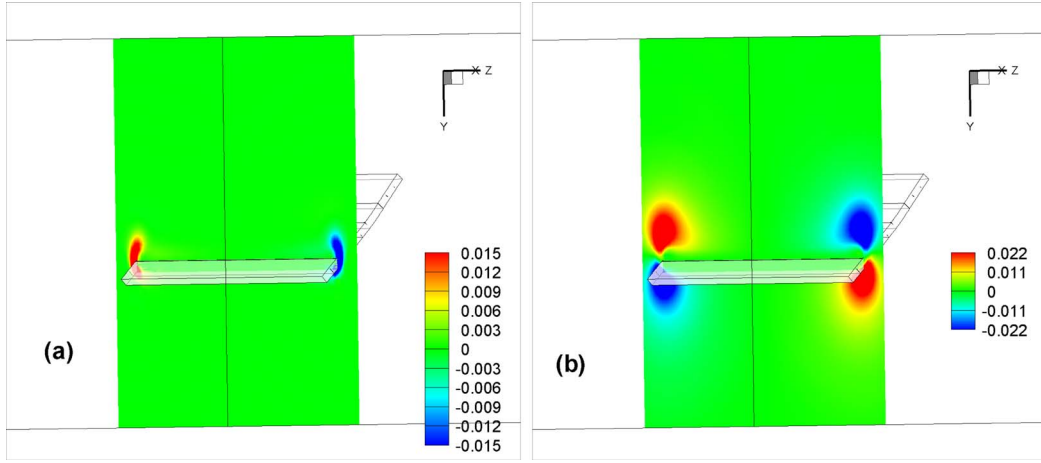


FIG. 14. The contours of (a) the vorticity in the chord-wise direction or the z-direction and (b) the velocity in the span-wise or x-direction on the cross section of chord ratio $r_p = 0.82$ are shown for base angle $\theta = 45^\circ$ (time instance $t = 1.36$) at a given $\kappa = 1.25$ and $EI = 0.67$.

The iso-surface of the vorticity magnitude is also shown in Figure 15 in a three-dimensional space. Some degree of the similarity of vortical structural patterns are observed between the current results and the results of Jantzen *et al.*¹⁸ for rigid wing. In this low Reynolds number range, the fluid flows are basically laminar with 3D tip vortices. The different vorticity patterns between the flexible and rigid wings are seen. It seems that the vortex separation along the wing tip areas is delayed for the flexible wing and the vortexes cover more the top chord surface, as shown in Figure 15.

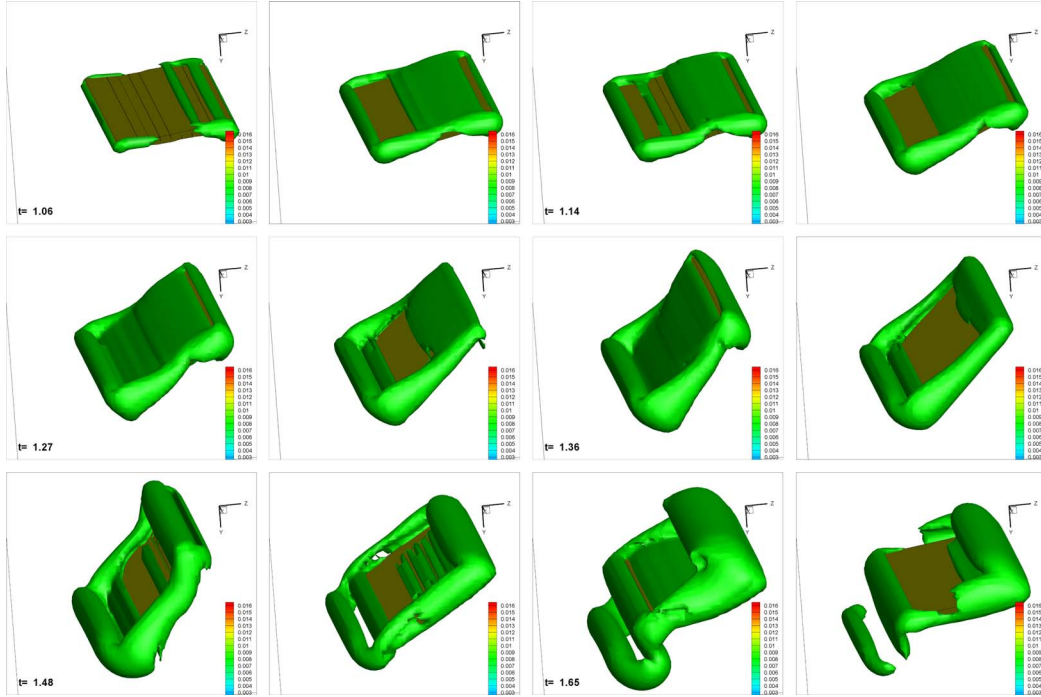


FIG. 15. The iso-surface of the vorticity magnitude are compared between the flexible wing (first and third columns) of $EI = 0.67$ and the rigid wing (second and fourth columns). The corresponding time instances or angles are the same as Figure 13. The value of the iso-surface is 0.008.

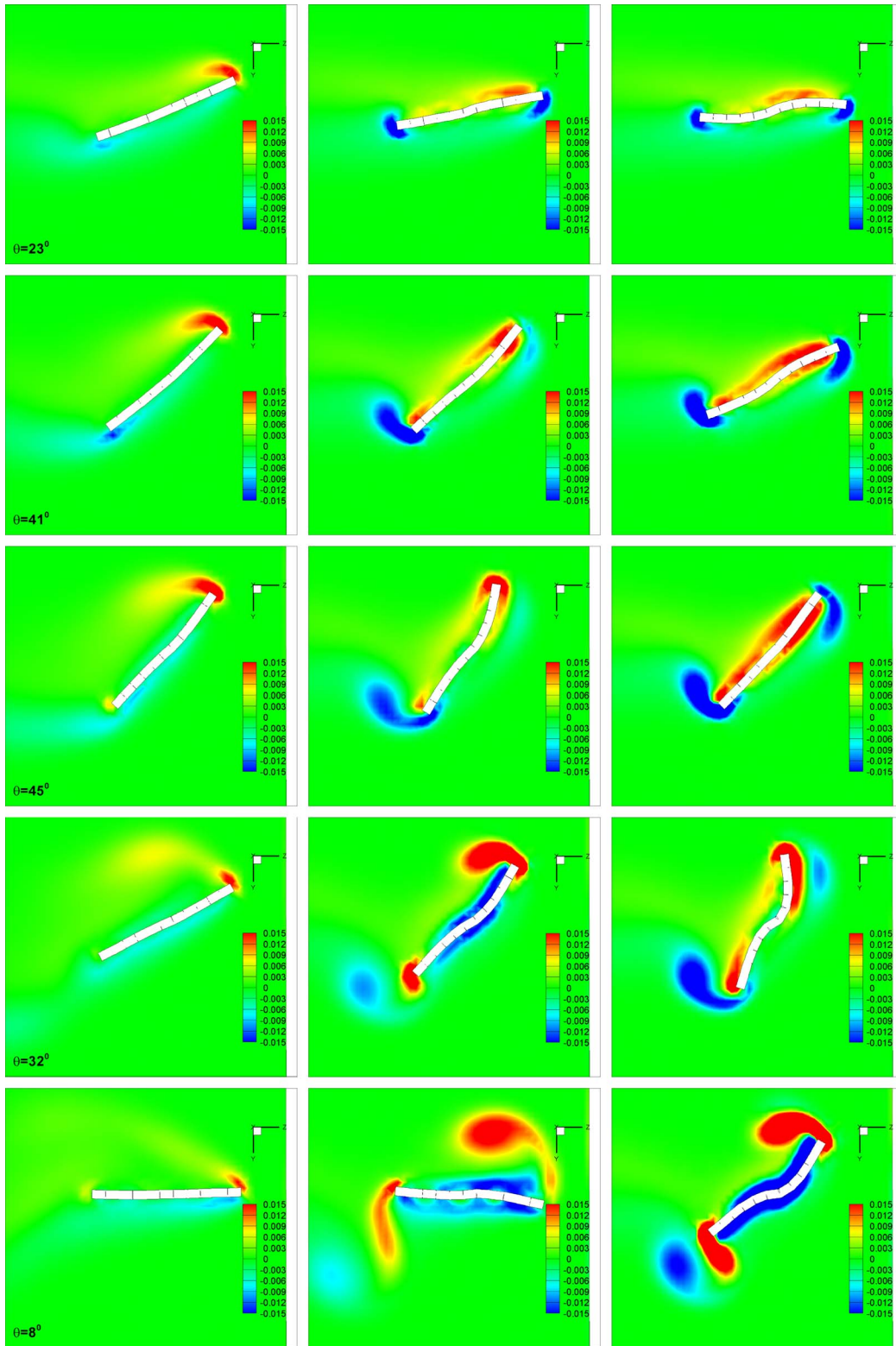


FIG. 16. The contours of the vorticity in the x-direction in the cross section at $s_r = 0.25$ are compared among different pitch rates $\kappa = 0.2$ (left column), 0.7 (middle column), and 1.25 (right column) of the flexible wing of $EI = 0.45$ at different base angles (time instances).

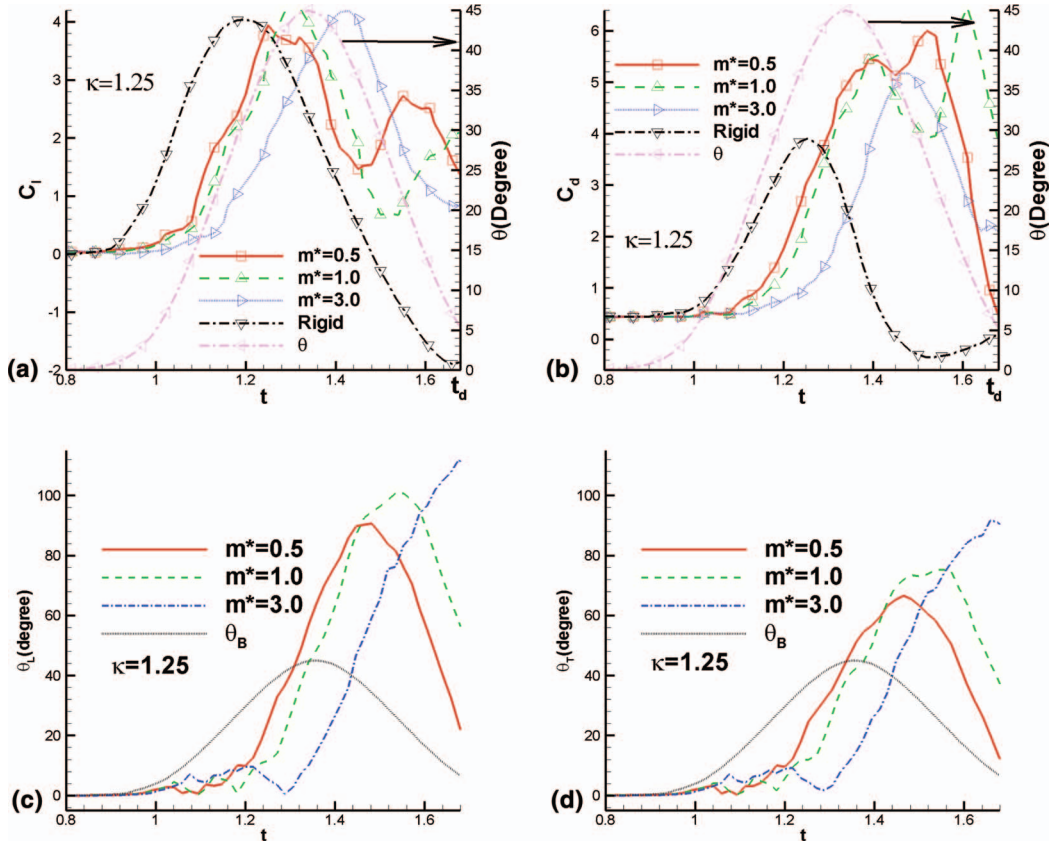


FIG. 17. The results of the lift (a), drag (b) coefficients, (c) the angle of the leading edge, (d) the angle of the trailing edge as a function of time are compared among different mass ratios at a given $EI = 0.45$ and a given pitch rate $\kappa = 1.25$.

In summary, the flexible wing has a larger angular momentum due to its elasticity and inertia, produces a larger LEV, delays the LEV separation, allows the vortices to cover a top chord surface area with a longer time and enhances the lift. This lift enhancement mechanism due to delayed LEV separation caused by large rotational momentum associated with flexibility is identified.

To elucidate the effects of pitch rate on vortical structures, the contours of the vorticity in the x -direction are displayed in Figure 16 for the three different levels of the pitch rate $\kappa = 0.2, 0.7$, and 1.25 at a given mass rate $m^* = 1.0$ and rigidity $EI = 0.45$. For $\kappa = 0.2$ case, the LEV are emanating from the leading edge and leave the top surface with a much larger distance for all the angles while for $\kappa = 0.7$ and 1.25 , the LEV stay a longer time on the top surface. For instance, at $\theta = 41^\circ$, the LEV is clearly separated for $\kappa = 0.2$ while the LEV attaches more closely to the top surface and the separated LEV is reattached on the top surface of the trailing edge portion for $\kappa = 0.7$. A larger LEV covers almost all top surface. Moreover, the TEV with an opposite sign are larger and curved up more as the pitch rate increases. The same occurs at $\theta = 45^\circ$. During the pitch-down, at $\theta = 32^\circ$ the separated LEV is reattached and covered more the top area of the trailing edge for $\kappa = 1.25$ and its larger TEV is rolled up more while the TEV are dispersed earlier for $\kappa = 0.7$ and 0.2 . Finally, it is seen that the structure of the vortices at $\theta = 8^\circ$ during the pitch-down for $\kappa = 1.25$ resembles those at $\theta = 32^\circ$ for $\kappa = 0.7$, depicting that the high pitch rate delays the LEV separation due to flexibility.

D. Effect of wing mass ratio

To study effect of wing mass, the mass ratios are varied in the three levels of $m^* = 0.5, 1.0$, and 3.0 , which are in the range of the insects density and used by other authors.²⁵

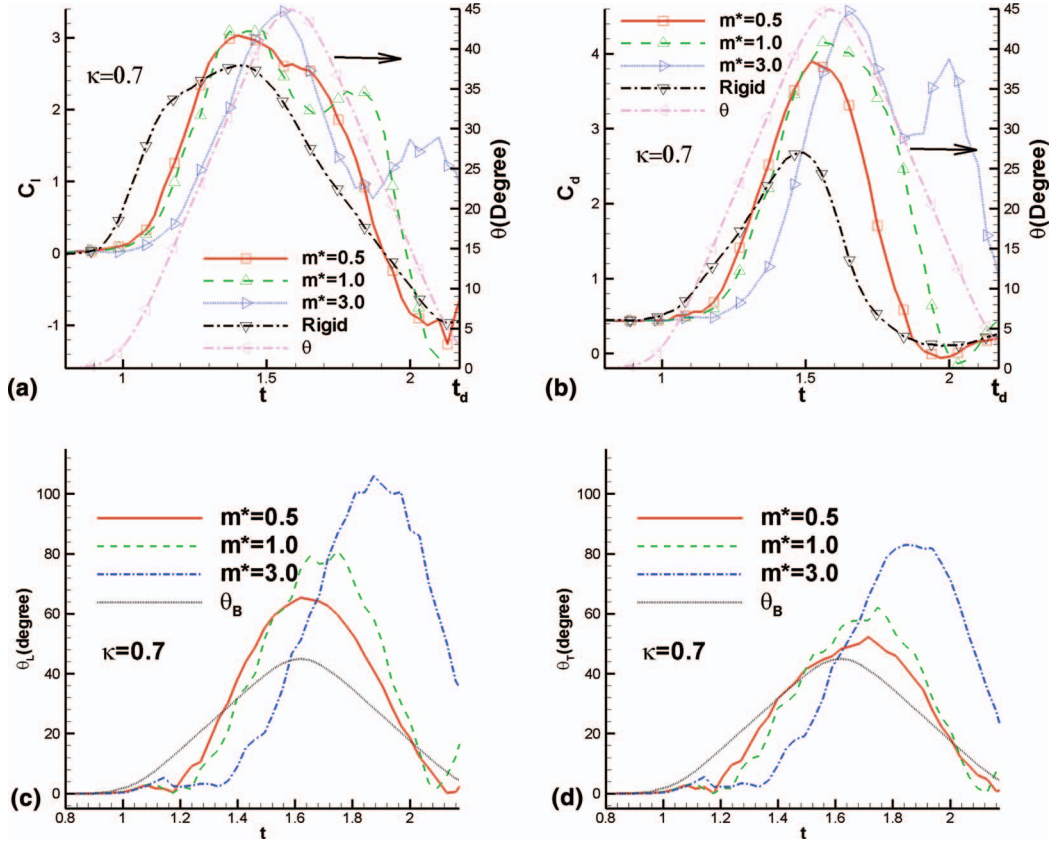


FIG. 18. The results of the lift (a), drag (b) coefficients, (c) leading edge angle and (d) trailing edge angle as a function of time are compared among different mass ratio at a given pitch rate $\kappa = 0.7$ and a given $EI = 0.45$.

For a given large rational rate $\kappa = 1.25$, the results of the lift and drag coefficients as a function of time are exhibited in Figure 17 for the flexible wing of $EI = 0.45$ at different levels of the mass ratios and compared with the rigid wing. Figure 17 shows that as the mass ratio increases from $m^* = 0.5$ to $m^* = 1.0$, the first maximum of the lift coefficient increases from 3.94 to 4.41 and the stall angle increases from $\theta_{st} = 39^\circ$ to $\theta_{st} = 44^\circ$. As the mass ratio continuously increases to $m^* = 3.0$, the first maximum of the lift reduces to 4.19, and the stall angle becomes $\theta_{st} = 39^\circ$. It seems that the largest stall angle and lift maximum are obtained for the intermediate mass ration $m^* = 1.0$. Importantly, the stall angles of the flexible wings with all three level mass ratios are larger than the stall angle 29° of the rigid wing.

In addition, two peaks are clearly presented in the force curves of the flexible wings of $m^* = 0.5$ and 1.0 and both the first and second peaks are delayed as the mass ratio increases from $m^* = 0.5$ to $m^* = 1.0$. It is understood that for a low mass ratio $m^* = 0.5$, the ratio of wing inertial to fluid hydrodynamic force is smaller. Therefore, the relatively smaller inertial and larger viscous damping forces cause smaller angular deformation as shown in Figures 17(c) and 17(d). As the mass ratio increases to $m^* = 1.0$, the wing inertial force is relatively larger and the fluid viscous damping is relatively smaller. Thus, a larger deformation is obtained and causes lift peaks delayed. As the mass ratio continuously increases to $m^* = 3.0$, the inertially dominated force drives the first peak greatly delayed and the second peak to be out of the time range of the pitch-down motion. The second peak looks like disappearance.

For an intermediate pitch rate $\kappa = 0.7$, the results of lift and drag forces and angular deformation are shown in Figure 18 and their behavior is similar to the case of $\kappa = 1.25$ except that the lift force is smaller for $\kappa = 0.7$ than for $\kappa = 1.25$.

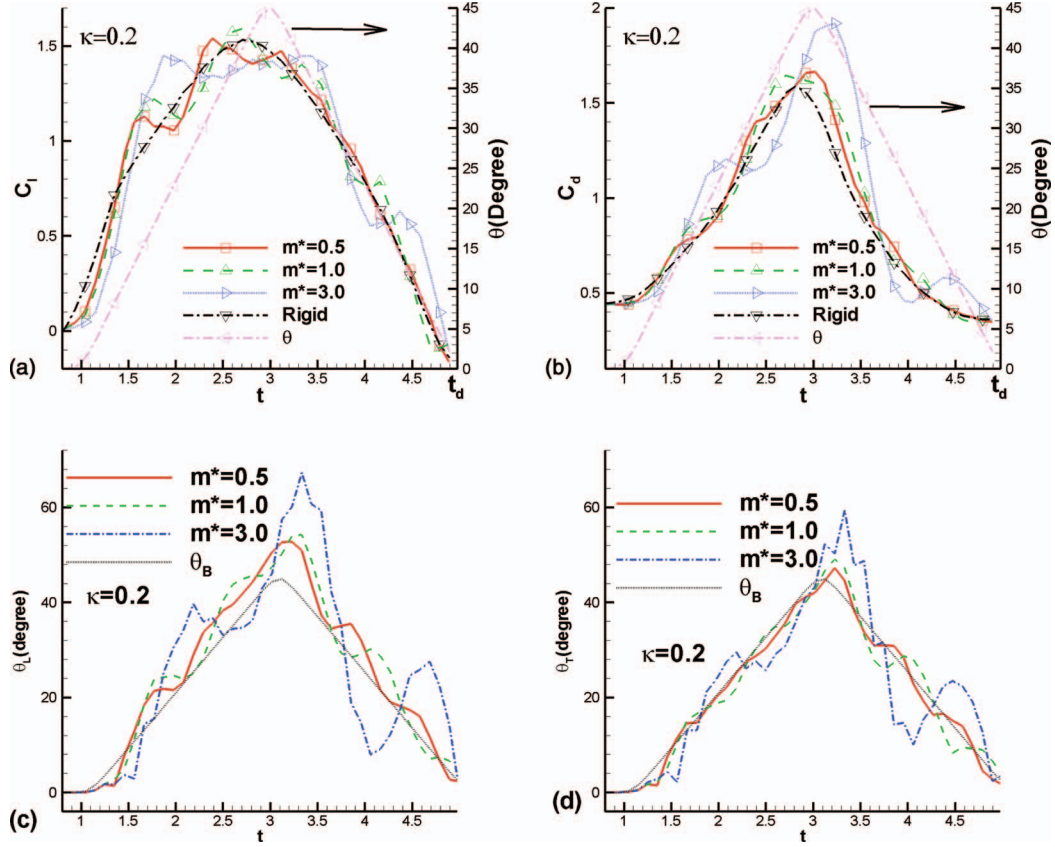


FIG. 19. The results of the lift (a), drag (b) coefficients, (c) leading edge angle, and (d) trailing edge angle as a function of time are compared among different mass ratios at a given pitch rate $\kappa = 0.2$ and a given rigidity $EI = 0.45$.

However, when the pitch rate is small at $\kappa = 0.2$, the situation is different. The results of lift and drag forces and deformation as a function of time are collected in Figure 19. No matter what mass ratio is, the stall angle and lift force are not larger for the flexible wing than for the rigid wing. It seems that the flexibility does not benefit lift nor stall angle at this low pitch rate.

Next, the results of the average lift and drag forces over time at a given pitch rate are displayed as a function of the rigidity at different wing mass ratio in Figure 20. For the case of $\kappa = 1.25$, all the lift coefficient curves have a maximum when the rigidity is at an intermediate level as shown in Figure 20(a). As the mass ratio increases, the lift force peak becomes much wider and the value of the maximum increases. In other words, the lift can be increased in a much larger range of the rigidity for a larger wing mass than a lower mass. This is caused by the larger inertial and less viscous damping force. For the case of $\kappa = 0.7$, the lift has a similar behavior except that the magnitude of lift is smaller than that of $\kappa = 1.25$ as shown in Figure 20(b). However, for a low pitch rate $\kappa = 0.2$, as shown in Figure 20(c) the lift curves are almost collapsed as one curve no matter what the mass ratio are, indicating that at this low pitch rate, the flexibility does not improve lift and the mass inertia may play an insignificant role. All the drag force curves have a peak. Generally speaking, the wing inertia benefits the lift at a large rotational rate.

E. Force asymmetry

To further distinguish the different effects of the flexibility on the pitch-up and on the pitch-down motion, the lift and drag coefficients are computed and averaged over the pitch-up time period between t_a and t_b and over the pitch-down time period between t_b and t_d , respectively, so that the force coefficient is reasonably divided into two portions: one called a pitch-up lift coefficient and

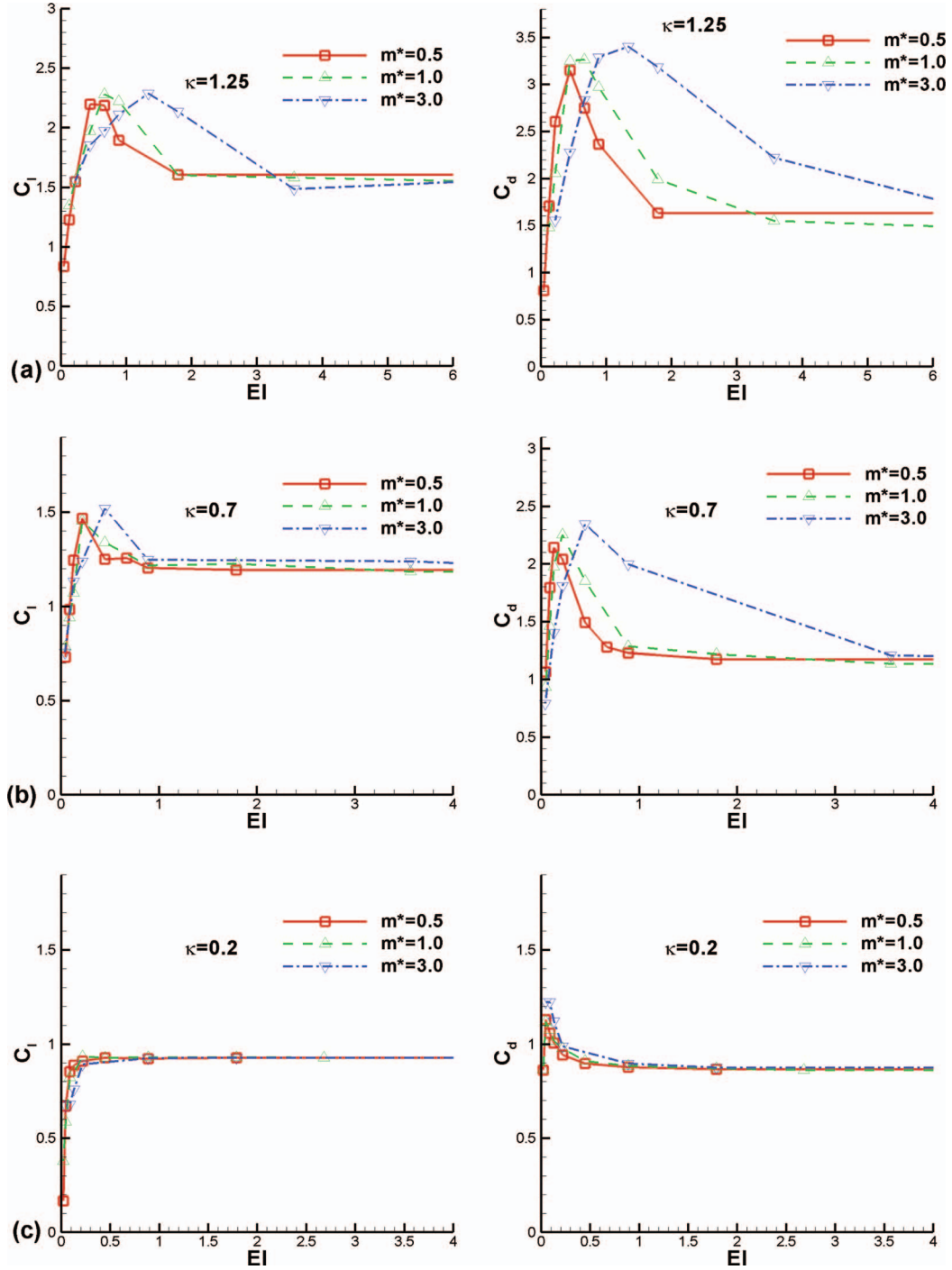


FIG. 20. The lift (left) and drag (right) coefficients as a function of rigidity at the pitch rates (a) $\kappa = 1.25$, (b) $\kappa = 0.7$, (c) $\kappa = 0.2$ for different wing mass ratio.

another called a pitch-down lift coefficient. The results of the pitch-up lift coefficients C_l^u , the pitch-down lift coefficient C_l^d , the pitch-up drag coefficient C_d^u , and the pitch-down drag coefficient C_d^d as a function of EI at different mass ratio are shown in Figure 21 for $\kappa = 1.25$, in Figure 22 for $\kappa = 0.7$, and in Figure 23 for $\kappa = 0.2$. The pitch-down lift coefficient C_l^d significantly increases as the rigidity decreases, arrives at a maximum, then falls down. There is a maximum as shown in

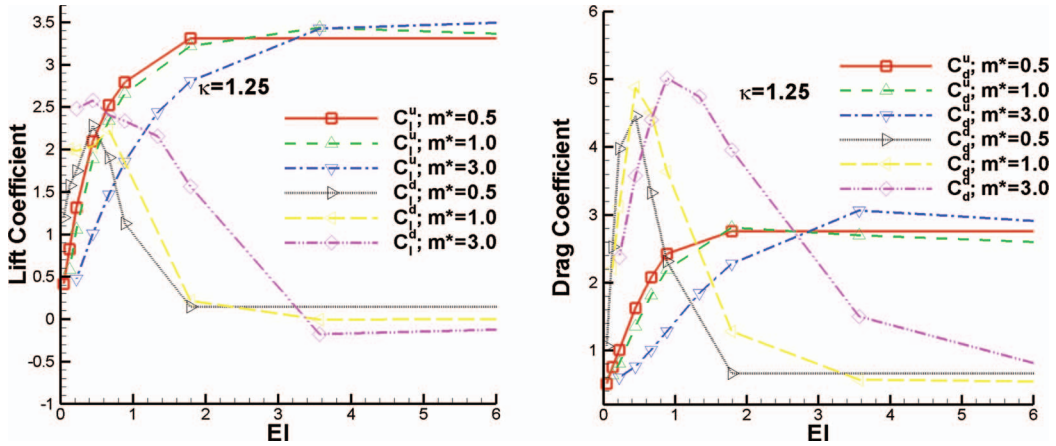


FIG. 21. The pitch-up lift coefficient C_l^u and the pitch-down lift coefficient C_l^d as well as the corresponding drag coefficients as a function of the rigidity for the case of $\kappa = 1.25$ at different mass ratios.

Figure 21 for $\kappa = 1.25$ and in Figure 22 for $\kappa = 0.7$. During the pitch-down motion, the flexibility can convert the pitch-down lift coefficient from a negative value -0.054 for the rigid wing to a positive value 2.23 for the flexible wing of $EI = 0.67$ for $\kappa = 1.25$, evidencing that the flexibility can dramatically improve lift during the pitch-down motion. By contraries, the pitch-up lift coefficient C_l^u monotonically decreases as the rigidity reduces. There is no maximum, i.e., the flexibility cannot improve the time average lift during the pitch-up period. However, it is special that a large lift maximum and a large stall angle always occur in the pitch-up period as shown in Figure 6 although its average lift is small. These results suggest that flexibility mainly contributes a larger lift during the pitch down motion and dominantly devotes a delayed stall angle during the pitch-up period. It is demonstrated that the lift force behavior due to flexibility is asymmetrical about the pitch-down motion and the pitch-up motion.

At the low pitch rate $\kappa = 0.2$, there is no maximum in both the pitch-down and pitch-up lift coefficient curves as shown in Figure 23. This is consistent with the finding in Sec. III B that the flexibility cannot enhance the lift at a low pitch rate. It is concluded that the lift force increase due to flexibility is dominated and driven by the pitch-down motion while a larger stall angle is mainly driven by the pitch-up motion. This asymmetrical property of the force increase may guide one to design an asymmetrical micro-vehicle with respect to the pitch-up motion and the pitch-down motion.

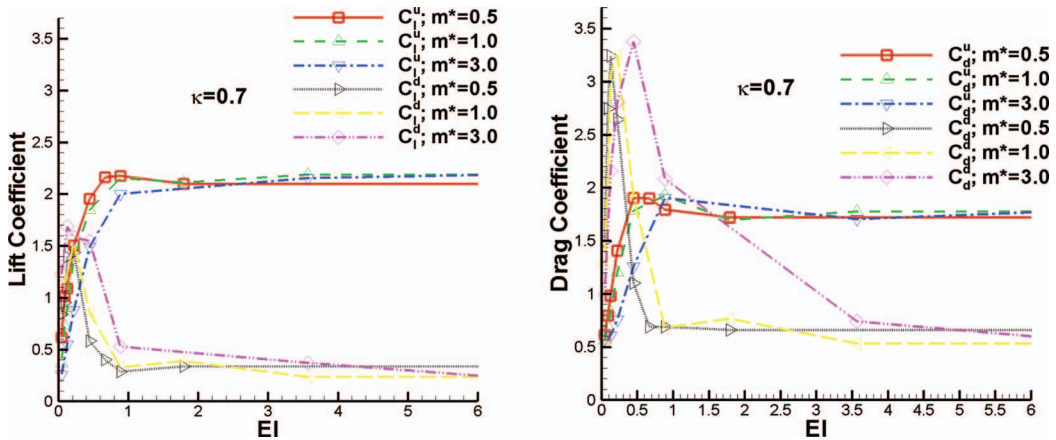


FIG. 22. The pitch-up lift coefficient C_l^u and the pitch-down lift coefficient C_l^d as well as the corresponding drag coefficients as a function of the rigidity for the case of $\kappa = 0.7$ at different mass ratios.

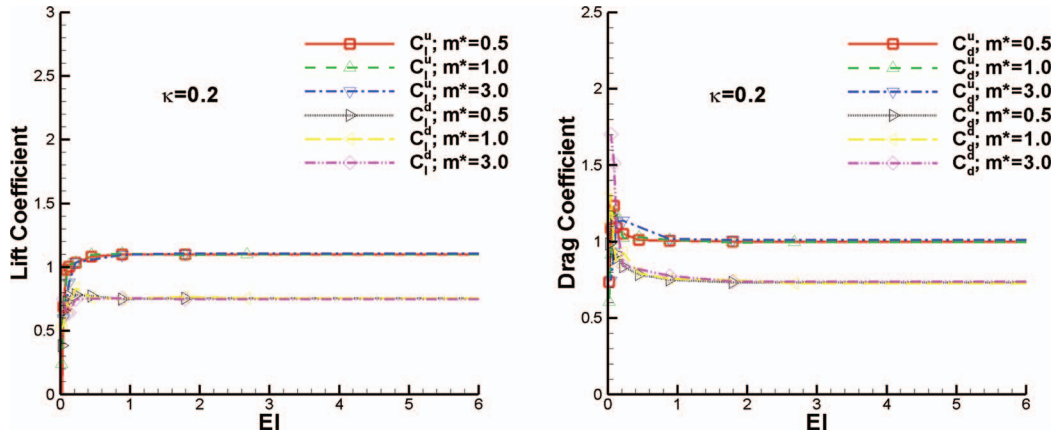


FIG. 23. The pitch-up lift coefficient C_l^u and the pitch-down lift coefficient C_l^d as well as the corresponding drag coefficients as a function of the rigidity for the case of $\kappa = 0.2$ at different mass ratios.

IV. CONCLUSION

The direct simulations of the pitch-up and pitch-down of the chord-wise flexible and rigid wings in a free stream are conducted at the Reynolds number of $Re = 100$ by using the LBFPM. The effect of the bending rigidity in the chord-wise direction on unsteady aerodynamics are investigated. Based on the comparison with the rigid wing, the following conclusions can be made.

- It is found that when the pitch rate is large, the lift and drag forces increase nonlinearly up to a maximum as the flexibility increases, then falls down as the flexibility becomes excessively large. The maximum values in both lift and drag forces are significantly larger for a flexible wing than for a rigid wing. It is the elastic restoring force with the inertia that generates a larger angular momentum, which produces a larger LEV, delays the LEV separation, stabilizes the LEV with a longer time to be attached on the top surface, and enhances lift force. This force enhancement mechanism due to large rotational momentum is identified for the flexible wing.
- It is found that the flexibility dominantly produces a large lift maximum and a large stall angle during pitch-up motion and devotes a large lift mainly during pitch-down motion. This force asymmetrical property may guide one to design an asymmetrical micro-vehicle with respect to the pitch-up motion and the pitch-down motion.
- Only when the rotational rate is larger than a critical rotational value, the flexibility can be used to improve lift.

ACKNOWLEDGMENTS

Dr. Qi acknowledges the support from the National Science Foundation (NSF) under Award No. 1126438; Dr. He would like to thank the financial supports from the National Natural Science Foundation of China (NNSFC) under Award No. 11232011 (Key project) and the National Basic Research Program of China (973 Program) under Award No. 2013CB834100.

¹J. Toomey and J. D. Eldredge, "Numerical and experimental study of the fluid dynamics of a flapping wing with low order flexibility," *Phys. Fluids* **20**, 073603 (2008).

²D. Qi, "Direct simulations of flexible cylindrical fiber suspensions in finite Reynolds number flows," *J. Chem. Phys.* **125**, 114901–114910 (2006).

³D. Qi, Y. Liu, W. Shyy, and H. Aono, "Simulations of dynamics of plunge and pitch of a 3D flexible wing in a low Reynolds number flow," *Phys. Fluids* **22**, 091901 (2010).

⁴D. Qi and Y. Liu, "Simulations of dynamics of plunge and pitch of a 3D chord-wise flexible wing in a low Reynolds number flow," in *Proceedings of the 49th AIAA Aerospace Sciences Meeting Including the New Horizons Forum and Aerospace Exposition, Orlando, Fl, 4–7 January 2011*, AIAA Paper 221.

⁵M. H. Dickinson, F. O. Lehmann, and S. Sane, "Wing rotation and the aerodynamic basis of insect flight," *Science* **284**, 1954–1960 (1999).

- ⁶C. P. Ellington, C. Berg Van de, A. P. Willmott, and A. L. R. Thomas, "Leading-edge vortices in insect flight," *Nature (London)* **384**, 626–630 (1996).
- ⁷M. V. Ol, A. Altman, J. D. Eldredge, D. J. Garmann, and Y. Lian, "Resume of the AIAA FDTC low Reynolds number discussion group's canonical cases," in *Proceedings of the 48th AIAA Aerospace Sciences Meeting Including the New Horizons Forum and Aerospace Exposition, Orlando, FL, January 2010*, AIAA Paper 1085.
- ⁸M. Ol, "The high-frequency, high-amplitude pitch problem: Airfoils, plates and wings," in *Proceedings of the 39th AIAA Fluid Dynamics Conference, San Antonio, TX, 2009*, AIAA Paper 3686.
- ⁹D. Williams, S. Buntain, V. Quach, and W. Kerstens, "Flow field structures behind a 3D wing in an oscillating freestream," in *Proceedings of the 39th AIAA Fluid Dynamics Conference, San Antonio, TX, 22–23 June 2009*, AIAA Paper 2690.
- ¹⁰Y. Lian, "Parametric study of a pitching flat plate at low Reynolds numbers," in *Proceedings of the 39th AIAA Fluid Dynamics Conference, San Antonio, TX, 2009*, AIAA Paper 3688.
- ¹¹J. D. Eldredge, C. Wang, and M. Ol, "A computational study of a canonical pitch-up, pitch-down wing maneuver," in *Proceedings of the 39th AIAA Fluid Dynamics Conference, San Antonio, TX, 2009*, AIAA Paper 3686.
- ¹²X. Zhang, S. Z. Ni, S. Z. Wang, and G. W. He, "Effects of geometric shape on the hydrodynamics of a self-propelled flapping foil," *Phys. Fluids* **21**, 103302 (2009).
- ¹³Y. Lian and M. V. Ol, "Experiments and computation on a low aspect ratio pitching flat plate," in *Proceedings of the 48th AIAA Aerospace Sciences Meeting Including the New Horizons Forum and Aerospace Exposition, Orlando, FL, January 2010*, AIAA Paper 0385.
- ¹⁴K. Kilany, C. Judde, and J. Soria, "Multi-component, multi-dimensional PIV measurements of low Reynolds number flow around a flat plate undergoing pitch-ramp motion," in *Proceedings of the 39th AIAA Fluid Dynamics Conference, San Antonio, TX, June 2009*, AIAA Paper 3692.
- ¹⁵M. V. Ol, J. D. Eldredge, and C. Wang, "High-amplitude pitch of a flat plate: An abstraction of perching and flapping," *Int. J. Micro Air Vehicles* **1**, 203 (2009).
- ¹⁶N. A. Buchmann, A.-J. Buchner, K. Kilany, C. Atkinson, and J. Soriad, "Multi-component, multi-dimensional PIV measurements of a flat-plate pitching motion," in *Proceedings of the 40th Fluid Dynamics Conference and Exhibit, Chicago, IL, 28 June–1 July 2010*, AIAA Paper 4278.
- ¹⁷T. O. Yilmaz and D. Rockwell, "Flow structure on finite-span wings due to pitch-up motion," *J. Fluid Mech.* **691**, 518–545 (2012).
- ¹⁸R. Jantzen, K. Taira, K. Granlund, and M. V. Ol, "On the influence of pitching and acceleration on vortex dynamics around low-aspect-ratio rectangular wings," in *Proceedings of the 51st AIAA Aerospace Sciences Meeting and Exhibit, Grapevine, TX, 10 July 2013*, AIAA Paper 833.
- ¹⁹M. R. Visbal, "Flow structure and unsteady loading over a pitching and perching low-aspect-ratio wing," in *Proceedings of the 42nd AIAA Fluid Dynamics Conference and Exhibit, New Orleans, LA, 25–28 June 2012*, AIAA Paper 3279.
- ²⁰D. Garmann and M. Visbal, "Numerical investigation of transitional flow over a rapidly pitching plate," *Phys. Fluids* **23**, 094106 (2011).
- ²¹M. R. Visbal and D. V. Gaitonde, "High-order accurate methods for complex unsteady subsonic flows," *AIAA J.* **37**, 1231–1239 (1999).
- ²²H. Goldstein, *Classical Mechanics* (Addison-Wesley Publishing Company, Cambridge, MA, 1980).
- ²³J. D. Eldredge and C. Wang, "High-fidelity simulations and low-order modeling of a rapidly pitching plate," in *Proceedings of the 40th Fluid Dynamics Conference and Exhibition, AIAA, Chicago, IL, June 2010*, AIAA Paper 4281.
- ²⁴C. J. Barnes and M. R. Visbal, "High-fidelity simulations of a hovering win," in *Proceedings of the 42nd AIAA Fluid Dynamics Conference and Exhibit, New Orleans, LA, 25–28 June 2012*, AIAA Paper 2699.
- ²⁵D. Hu, H. Luo, and J. F. Doyle, "Dynamic pitching of an elastic rectangular wing in hovering motion," *J. Fluid Mech.* **693**, 473–499 (2012).
- ²⁶J. M. Gere and S. P. Timoshenko, *Mechanics of Materials*, 2nd ed. (Van Nostrand Reinhold, 1987).